Dynamic Calibration of GPS Effective Isotropic Radiated Power for GNSS-Reflectometry Earth Remote Sensing

Tianlin Wang, *Member, IEEE*, Christopher S. Ruf, *Fellow, IEEE*, Scott Gleason, *Senior Member, IEEE*, Andrew J. O'Brien, *Member, IEEE*, Darren S. McKague, *Member, IEEE*, Bruce P. Block, and Anthony Russel

Abstract—Global Navigation Satellite System (GNSS) Reflectometry uses reflected GNSS signals for Earth remote sensing applications. Absolute calibration of a Delay Doppler Map (DDM) requires an accurate estimate of the effective isotropic radiated power (EIRP) of the GNSS transmitter, e.g., Global Positioning System (GPS). However, variable transmit power by numerous Block II Follow-on (IIF) and II Replenishment-Modernized (IIR-M) GPS space vehicles has been observed due to their flex power mode. Nonuniformity in the GPS antenna gain patterns further complicates EIRP estimation. A dynamic calibration approach is developed to address GPS EIRP variability. It uses measurements by the direct received GPS signal to estimate GPS EIRP in the specular reflected direction and then incorporates it into the calibration of normalized bistatic radar cross section (NBRCS). Error analyses using Monte Carlo simulations and a root sum of squares (RSS) approach show that the resulting error in NBRCS is about 0.32 dB. Dynamic EIRP calibration instantaneously detects and corrects for power fluctuations in the GPS transmitters and significantly reduces errors due to GPS antenna gain azimuthal asymmetry. It allows observations with the most variable Block IIF transmitters (approximately 37% of the GPS constellation) to be included in the standard data products and further improves the calibration quality of NBRCS and geophysical data products.

Index Terms—Bistatic radar, calibration, Cyclone Global Navigation Satellite System (CYGNSS), effective isotropic radiated power (EIRP), flex power, Global Navigation Satellite System-Reflectometry (GNSS-R), Global Positioning System (GPS), remote sensing.

Tianlin Wang is with the Department of Electrical Engineering and Computer Science, University of Michigan, Ann Arbor, MI 48109 USA (e-mail: wangtl@umich.edu).

Christopher S. Ruf is with the Department of Climate and Space Sciences and Engineering, University of Michigan, Ann Arbor, MI 48109 USA, and also with the Department of Electrical Engineering and Computer Science, University of Michigan, Ann Arbor, MI 48109 USA (e-mail: cruf@umich.edu).

Scott Gleason is with the Constellation Observing System for Meteorology, Ionosphere, and Climate Program (COSMIC), University Corporation for Atmospheric Research, Boulder, CO 80307 USA (e-mail: gleason@ucar.edu).

Andrew J. O'Brien is with the ElectroScience Laboratory, Department of Electrical and Computer Engineering, The Ohio State University, Columbus, OH 43210 USA (e-mail: obrien.200@osu.edu).

Darren S. McKague is with the Department of Climate and Space Sciences and Engineering, University of Michigan, Ann Arbor, MI 48109 USA (e-mail: dmckague@umich.edu).

Bruce P. Block is with the Space Physics Research Laboratory, University of Michigan, Ann Arbor, MI 48109 USA (e-mail: bpblock@umich.edu).

Anthony Russel is with the Space Physics Research Laboratory, University of Michigan, Ann Arbor, MI 48109 USA (e-mail: russelan@umich.edu).

Digital Object Identifier 10.1109/TGRS.2021.3070238

I. INTRODUCTION

GLOBAL Navigation Satellite System (GNSS) provides positioning, navigation, and timing (PNT) services on a global basis [1], [2]. GNSS-Reflectometry (GNSS-R) uses the reflected GNSS signals from the Earth surface for remote sensing applications [3]. Most current and future GNSS-R spaceborne missions use the Global Positioning System (GPS) as an active source. An aircraft experiment demonstrated that GNSS-R could be used to sense ocean surface roughness and wind speed [4], [5]. More elaborate airborne GNSS-R campaigns were conducted to measure various geophysical parameters of the Earth environment, including the retrieval of wind speed above rough seas [6], [7], the mean square slope of the ocean surface [8], and wind speed in tropical cyclones [9], [10]. GNSS-R instruments were developed and launched into space with the following satellite missions: U.K. Disaster Monitoring Constellation (DMC) [11], [12], TechDemoSat-1 (TDS-1) [13], NASA Cyclone Global Navigation Satellite System (CYGNSS) [14], [15], [3]Cat-2 [16], BuFeng-1 A/B [17], Spire CubeSats [18], and Federated Satellite Systems Cube-Sat Assessment and Test (FSSCat) [19]. The spaceborne GNSS-R measurements have demonstrated that they provide accurate geophysical retrievals, including: 1) sea surface height [20], [21], wind speed in tropical cyclones [22]–[24] as well as global winds [25], [26], and swell waves over ocean surface [27]–[29]; 2) soil moisture content [30]–[33], biomass [34], [35], flood inundation [36], [37], and wetland dynamics [38], [39] over the land surface; and 3) sea ice [40], [41] and glaciers in the cryosphere [42], [43].

The typical GNSS-R observables are the delay waveforms and Delay Doppler Maps (DDMs). The intensity of every DDM pixel is proportional to the scattered power originating from the surface. Early retrieval algorithms for airborne GNSS-R experiments [6] use the trailing edge slope and the complete shape of the waveform and compare against analytical models based on geometric optics (GO) [8]. A similar approach was developed by minimizing a cost function of the model-generated delay waveforms under different wind speeds and the measured waveform computed from the raw data sets for the U.K. DMC mission [11]. These waveform-based approaches do not require absolute calibration of the received power and the retrievals are only dependent on the shape

of the waveform. On airborne platforms, these approaches use portions of the DDM that correspond to scattering from areas on the surface of a few km^2. However, at spaceborne altitudes and velocities, the same delay and Doppler ranges can correspond to surface areas of one hundred or more km^2. This would significantly degrade the spatial resolution and scientific value of geophysical data products derived from the measurements. Well calibrated normalized bistatic radar cross section (NBRCS) measurements will also provide more physical insight into the scattering mechanism for in-depth studies of ocean surface processes and their relation to the wind- and swell-generated waves.

A different series of retrieval approaches was based on use of the bistatic radar cross section (BRCS) derived from the DDMs. A model-based algorithm was developed for the U.K. DMC experiment by matching measured BRCS with model predictions, although erroneous assumptions made about the transmitters did introduce calibration errors [44]. The TDS-1 mission uses the average BRCS to retrieve wind speed, with an assumption that BRCS is constant over the glistening zone. An empirical geophysical modeling function (GMF) is generated by collocating the averaged BRCS measurements with the European Centre for Medium-range Weather Forecasts (ECMWF) wind. It has been demonstrated that the accuracy of wind speed retrieval is significantly impacted by the calibration quality of the BRCS observable [45].

The CYGNSS mission also uses empirical GMFs derived from the CYGNSS observables, including NBRCS and the leading edge slope (LES) of the delay waveform, which are nearly coincident with independent estimates of the Modern-Era Retrospective analysis for Research and Applications, Version 2 (MERRA-2) wind speed. By linearizing the GMF, it is shown that the component of wind speed error due to measurement error will be large for high wind speeds. This indicates that in the regime of high wind speed, the calibration quality of the NBRCS and LES observables is extremely important to the accuracy of the wind speed retrieval [46], [47].

One of the key parameters used in the calibration of NRBCS is the effective isotropic radiated power (EIRP) of the Global Navigation System (GPS) satellites, defined as the product of transmit power and antenna gain. It determines the exact power density incident on the Earth surface and, therefore, knowledge of it is very significant to the calibration quality [48]. The major challenges in the estimate of the GPS EIRP are presented in [49] and summarized here: 1) the variation of the transmit power; 2) limited knowledge of the transmit antenna gain pattern; and 3) the gain uncertainty due to pattern asymmetry and spacecraft yaw maneuvers. The CYGNSS version 2.1 (v2.1) Level 1b (L1b) calibration algorithm makes the following assumptions to determine the GPS EIRP in the direction of the specular reflection point: 1) static values for the effective GPS transmit power (L1 C/A code), as estimated using a GPS constellation power monitor (GCPM) system [50]; and 2) estimate of the GPS transmit antenna gain in the direction of the specular reflection point using an off-boresight azimuthal averaged estimate of the individual GPS transmitters, based on the publicly available prelaunch

measured patterns of Block II Replenishment (IIR) and IIR-Modernized (IIR-M) satellites provided by Lockheed-Martin [51] and release controlled prelaunch pattern estimates for the Boeing Block II Follow-on (IIF) satellites. This approach has proved successful at reducing the CYGNSS data products' dependence on the block type and individual space vehicle (SV) of the GPS transmitter for all but the Block IIF SVs [52]. The variability in transmit power with Block IIF is unacceptably large and they have been screened out of the v2.1 data release for that reason.

However, there are still remaining issues in the estimate of the GPS EIRP, including 1) existing errors in the estimated transmit power; 2) flex transmit power of the GPS Block IIR-M and IIF SVs [53], [54]; and 3) inaccurate estimate of the GPS transmit antenna gain due to the azimuthal asymmetry of its gain pattern. More details are discussed in Section II. To address these issues, a dynamic calibration approach is developed which uses the CYGNSS direct (zenith) channel to estimate the GPS EIRP in the direction of the specular reflection point [55]. By incorporating the calibrated EIRP into the CYGNSS L1b algorithm, this approach recovers all flagged observations from the GPS Block IIF to be included in the standard science data products and further improves the data quality of NBRCS.

The outline of this article is as follows. Section II reviews the challenges in estimating the GPS EIRP and the motivation of this research. Section III presents the methodology and algorithm. Section IV discusses the error analysis of the calibration algorithm. Section V shows the results, including the estimated GPS EIRP and the impact on the CYGNSS NBRCS. Section VI discusses future improvement plans and summarizes this article.

II. MOTIVATION

Current operational GPS satellites have 4 different block types of SVs, including 8 IIR, 7 IIR-M and 12 IIF, and 4 III. Among these, the IIR, IIR-M, and III SVs were built by Lockheed Martin and the IIF SVs were built by Boeing. Differences in the design and manufacturing of the SVs and, in particular, in the transmitted power and transmit antenna patterns introduce corresponding differences in the GPS EIRP, which, if not properly accounted for, increase the uncertainty of the measurement.

One primary determiner of EIRP is the GPS transmit power. According to GPS specifications, the power referenced to the transmit antenna input port is at least 14.3 dBW (27 watts). However, typical GPS satellites broadcast 2–4 dB more power than that value. Previous studies show that there are differences in the GPS transmit power of individual IIR block-type satellites [50]. Second, and more importantly, a flex power mode of the Block IIR-M and IIF GPS satellites was developed and implemented to redistribute the transmit power between the individual signal components of the C/A, P(Y), and M codes for increased protection against jamming in certain regions. On February 7 and 8, 2017, 7 active IIR-M satellites performed a commanded redistribution of transmit power from M code to C/A and P(Y) codes. From January 27, 2017 to February 13, 2020, Block IIF GPS satellites have
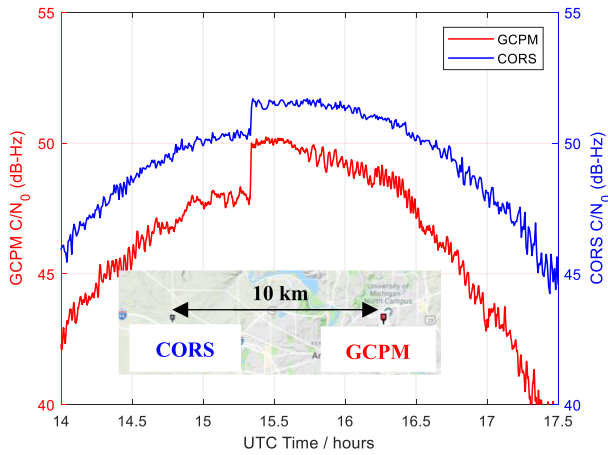
Fig. 1. Flex power of GPS SVN 63 (Block IIF) observed by two independent ground-based GPS receivers, GCPM and NOAA CORS, separated by a distance of ∼10 km based on the inserted Google Map.

implemented a geographically driven flex power mode, which enables a ∼2.5 dB increase and decrease in the L1 C/A code's power with every orbit [54]. This flex power mode was simultaneously observed by the GCPM [50] and a local GPS Continuously Operating Reference Station (CORS) by National Oceanic and Atmospheric Administration (NOAA), as shown in Fig. 1. The carrier-to-noise ratio (C/N_0) has increased more than 2 dB for both systems. The difference between the C/N_0 levels is caused by the different configurations of the two GPS receivers, including the receiver system gain, the setting of automatic gain control (AGC), and so on. The significant power increase and decrease over several seconds repeat at the same geographical location over consecutive days.

If an abrupt change of transmit power is not properly accounted for, it will introduce a corresponding change in the Level 1 NRBCS. This is a calibration error due to the flex power event. Such unpredictable flex power events prevent us from assigning a correct transmit power level for Block IIF satellites. Therefore, observations from all IIF satellites are flagged out in the v2.1 data set. This reduces the CYGNSS measurement coverage by approximately 37% and affects the revisit time of the mission. This will limit the mission's potential in many high-level scientific applications, for example, tracking hurricane intensity and flood inundation after landfall, resolving diurnal variations in ocean surface winds and heat flux, and capturing the rapid dry down response of soil moisture to extreme precipitation events.

The second primary determiner of EIRP is the transmit antenna gain. The gain is defined as the product of the directivity and the gain correction factor (GCF). However, only the 20 antenna patterns of block-type 12 IIR and 8 IIR-M satellites have been published in [51], while those of 12 IIF and 4 III satellites have not been publicly released. The published prelaunch measured antenna patterns are not sufficient for the CYGNSS Level 1 calibration because: 1) the on-orbit GPS transmit antenna gain patterns are known to differ from the prelaunch measured patterns, as the prelaunch measurements were not made while mounted on the flight SV. This would result in pattern distortions as the antenna interacted with the spacecraft and additional avionics present on the same face as the GPS transmit antenna; 2) the resolution of the published

patterns is low, 2° in off-boresight angle and 10° in around-boresight angle; and 3) the azimuthal asymmetry of GPS antenna gain brings additional error if using an off-boresight azimuthal averaged estimate or if not properly corrected for spacecraft yaw attitude maneuvers [56], [57]. The limited knowledge and possible measurement error of the directivity reduce confidence in the estimate of antenna gain and, thus, the GPS EIRP.

An absolute calibration algorithm would require replacement of simple off-boresight models with full GPS antenna pattern estimates and GPS satellite yaw state modeling for each transmitter. It is extremely difficult to estimate the full pattern using limited ground-based GPS receivers. Also, knowledge of the GPS satellite orientation is complicated by its recurring yaw maneuvers. It is possible but would be rather cumbersome to implement and would increase data latency in order to obtain the necessary GPS satellite yaw states.

To summarize, a calibration technique is needed to solve or mitigate the above two issues with GPS EIRP knowledge. It should be able to 1) detect and correct for power fluctuations in all GPS transmitters and 2) reduce calibration errors due to the azimuthal asymmetry of the GPS antenna gain pattern.

III. METHODOLOGY

A. Overview of the Dynamic EIRP Calibration

CYGNSS Level 1a (L1a) calibration converts each bin in the Level 0 DDM from raw counts to units of watts. Then, the CYGNSS L1b calibration generates two data products associated with each L1a DDM: 1) a bin-by-bin calculation of the surface BRCS, or σ, and 2) bin-by-bin values of the effective scattering areas. With other metadata, these two intermediate variables are used to compute the NBRCS [58] as

$$\bar{\sigma}\left(\hat{\tau}, \hat{f}\right) = \frac{P_g\left(\hat{\tau}, \hat{f}\right)(4\pi)^3 \left(R^T\right)^2 \left(R^R\right)^2}{E_S \lambda^2 G_S^R} \tag{1}$$

where $P_g\left(\hat{\tau}, \hat{f}\right)$ is the L1a calibrated signal power at a specific delay ($\hat{\tau}$) and Doppler ($\hat{f}$) bin, R^T is the range from the transmitter to the surface, R^R is the range from the surface to the receiver, E_S is the GPS EIRP in the direction of the specular reflection point, λ is the wavelength for GPS L1 signals, and G_S^R is the receiver antenna gain at the specular point.

Dynamic EIRP calibration uses measurement made by the CYGNSS direct (zenith) channel to solve for GPS EIRP in the direction of the zenith antenna (E_Z). E_S is then estimated from E_Z and a correction is made to the Level 1 NBRCS calibration. The measurement geometry is illustrated in Fig. 2.

In this way, 8 CYGNSS zenith receivers are converted into 8 real-time GPS power monitor systems. By making direct, temporally coincident estimates of the GPS EIRP, this dynamic EIRP calibration algorithm can instantaneously detect and correct for power fluctuations in all GPS block transmitters. This approach also reduces errors due to GPS antenna gain azimuthal asymmetry because the azimuthal angles of the zenith and nadir propagation paths are the same.

B. Calibration of the CYGNSS Zenith Signal

The zenith channel of the GPS receiver on CYGNSS was originally intended for navigation only, so there was no calibration capability included to convert the raw counts of
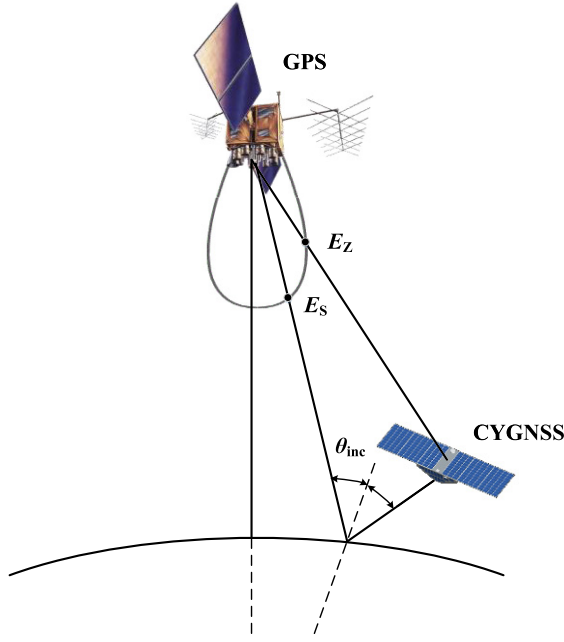
Fig. 2. Concept of the dynamic EIRP calibration algorithm (GPS antenna nominally points toward center of Earth). E_Z and E_S are the GPS EIRP in the direction of the CYGNSS satellite and the specular reflection point, respectively.

the direct navigation signal into power in watts. In addition, the zenith channel contains an AGC feature. Although the AGC ensures a consistent signal power level for navigation data processing purposes, the state of the AGC at any given time is not recorded by the receiver, which prohibits calibration of the direct-path GPS signal power. As of August 1, 2018, the AGC feature was disabled on all 8 CYGNSS flight models (FMs) and a constant gain value was used instead. Prior to this change, the ability to perform navigation functions properly over the full dynamic range of expected signal levels was verified.

Calibration of the zenith navigation receiver for power measurements was done using an engineering model (EM) of the CYGNSS receiver together with a GPS signal simulator (GSS) to emulate the on-orbit measurements [59]. A second-order power series expression was determined from the EM+GSS measurements, as given in Table I. It converts the raw counts ($C_Z = I_Z^2 + Q_Z^2$ in dB) measured by the zenith channel of the receiver, which is computed from the in-phase (I_Z) and quadrature-phase (Q_Z) components, into power referenced to the input port of the receiver (P_Z is originally computed in dB watts and then converted into a linear scale) as given by

$$P_Z = aC_Z^2 + bC_Z + c. \qquad (2)$$

The received power referenced to the output port of the zenith navigation antenna, P_R, can be determined from P_Z after correcting for the gain of the zenith low noise amplifier (LNA) G_{LNA} according to

$$P_R = \frac{P_Z}{G_{LNA}(T_{LNA})} \qquad (3)$$

TABLE I
ZENITH COUNTS TO POWER CONVERSION COEFFICIENTS

Coefficient	Value
a	0.011897122540965
b	-0.509944684931564
c	-1.511603333176575e+02

where T_{LNA} is the temperature of the LNA. G_{LNA} is calculated using a prelaunch lookup table (LUT) of gain versus physical temperature.

C. Characterization of CYGNSS Zenith Antenna Pattern

The accuracy of the estimated GPS EIRP depends on knowledge of the CYGNSS zenith antenna gain pattern, $G_R(\theta, \phi)$. Prior to launch, antenna measurements were performed in an anechoic chamber using a zenith antenna installed on an approximate CYGNSS satellite mock-up. Those measurements indicated that the antenna pattern was extremely sensitive to coupling and multipath from nearby satellite structures (e.g., the solar panels and other electrical elements) which were not deployed or positioned with sufficient repeatability between spacecraft. For this reason, it was concluded that the chamber measurements would be inadequate to accurately represent the CYGNSS zenith antenna patterns on the actual satellites and an on-orbit determination of the patterns would be necessary.

The CYGNSS zenith antennas were characterized on-orbit using a large collection of CYGNSS measurements of the direct GPS signal strength made by a subset of the GPS satellites for which the transmit power level does not change appreciably over time. Individual CYGNSS antenna gain patterns were determined for each of the eight satellites, as described in [59]. One example of the resulting pattern (for CYGNSS FM 1) is shown in Fig. 3(a). Since the CYGNSS receivers only record direct measurements from GPS satellites for which a reflected measurement is also made, the measurement density used to estimate the antenna patterns is not uniformly distributed across the pattern. An example measurement density is shown in Fig. 3(b). Only portions of the antenna pattern with high sampling density are used for Level 1 calibration of the reflected signal.

D. Estimating GPS EIRP Toward the CYGNSS Satellite

The Friis transmission equation can be rearranged to solve for E_Z, the GPS satellite EIRP in the direction of the CYGNSS satellite, as

$$E_Z = \frac{(4\pi R)^2}{\lambda^2} \frac{P_R}{G_R(\theta_R, \phi_R)} \qquad (4)$$

where R is the range from the GPS satellite to the CYGNSS satellite, $\lambda = 0.19$ m is the GPS signal wavelength, P_R is the received power of the GPS signal as calculated by (3), G_R is the gain pattern of the receive antenna, and θ_R and ϕ_R are the off-boresight and azimuthal angles of the GPS satellite in the receive antenna reference frame.
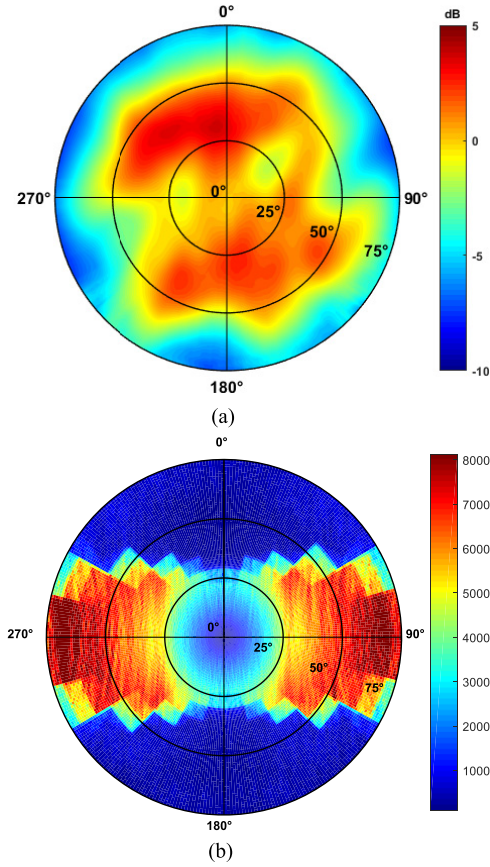
(a)

(b)

Fig. 3. (a) Gain pattern of the CYGNSS FM 1 zenith antenna that receives direct GPS signals. (b) Sampling density of direct-signal GPS measurements used to estimate the zenith antenna gain pattern.

E. Zenith-to-Specular Ratio (ZSR) Function

The time varying EIRP for a particular GPS satellite is the product of its transmit power P_T at time t and its realized antenna gain $G_T(\theta, \phi)$

$$E(t, \theta, \phi) = P_T(t)G_T(\theta, \phi) \tag{5}$$

where the elevation and azimuth angles (θ, ϕ) specify a direction in the GPS antenna reference frame.

For the geometric arrangement of the GPS satellite, CYGNSS satellite, and specular reflection point depicted in Fig. 2, we define the zenith-to-specular ratio (ZSR) as the ratio of the GPS EIRP in two specific directions

$$\text{ZSR} \triangleq \frac{E_Z}{E_S} = \frac{E(t, \theta_Z, \phi_Z)}{E(t, \theta_S, \phi_S)} \tag{6}$$

where (θ_Z, ϕ_Z) is the direction to the CYGNSS satellite and (θ_S, ϕ_S) is the direction to the specular reflection point.

Ultimately, our goal is to determine E_S, the GPS EIRP in the direction of the specular reflection point, from measurements of E_Z, the GPS EIRP in the direction of the CYGNSS satellite. To accomplish this, we develop an approximation of the ZSR function, $\widehat{\text{ZSR}}$, and use it to scale E_Z, as given by

$$E_S \simeq \frac{E_Z}{\widehat{\text{ZSR}}}. \tag{7}$$

The derivation of $\widehat{\text{ZSR}}$ is detailed below.

To begin, substituting (5) into (6) removes the dependence on GPS transmit power. The ZSR is equal to the time-independent ratio of GPS antenna gain in two directions, or

$$\text{ZSR}(\theta_Z, \theta_S, \phi_Z, \phi_S) = \frac{P_T(t)G_T(\theta_Z, \phi_Z)}{P_T(t)G_T(\theta_S, \phi_S)} = \frac{G_T(\theta_Z, \phi_Z)}{G_T(\theta_S, \phi_S)}. \tag{8}$$

Next, two approximations are made to simplify the form of (8). First, it is observed that, for specular reflection geometries, the azimuth angles ϕ_Z and ϕ_S are nearly identical. Therefore, we can rewrite the ZSR as a function of a single azimuth angle ϕ, or

$$\text{ZSR}(\theta_Z, \theta_S, \phi_Z, \phi_S) \simeq \text{ZSR}(\theta_Z, \theta_S, \phi) \tag{9}$$

where $\phi = \phi_Z = \phi_S$.

Second, it is observed that both of the elevation angles, θ_Z and θ_S, are (within a small fraction of a degree) related in a one-to-one fashion to the specular incidence angle θ_{inc}, or

$$\theta_Z \simeq \theta_Z(\theta_{\text{inc}}) \tag{10}$$

$$\theta_S \simeq \theta_S(\theta_{\text{inc}}). \tag{11}$$

Note that the relationships in (10) and (11) are only valid for a limited range of CYGNSS satellite altitudes. As CYGNSS satellite altitudes change over the life of the mission, the functional relationships may need to be recalculated. Using (10) and (11), the ZSR is approximated as

$$\text{ZSR}(\theta_Z, \theta_S, \phi_Z, \phi_S) \simeq \frac{G_T(\theta_Z(\theta_{\text{inc}}), \phi)}{G_T(\theta_S(\theta_{\text{inc}}), \phi)}. \tag{12}$$

At this point, the ZSR is expressed as a function of two parameters, the specular incidence angle, θ_{inc}, and the azimuthal angle of the specular reflection point in the GPS antenna reference frame, ϕ. If one examines the published GPS antenna patterns, they can be seen to exhibit significant variation in both elevation and azimuth. However, the relative dependence of gain on elevation at a fixed azimuth angle does not change significantly with azimuth. For that reason, the ZSR function is more weakly dependent on azimuth angle than is the gain itself. This suggests that the azimuthally dependent ZSR function in (12) can be approximated by its average value over all azimuth angles, as given by

$$\widehat{\text{ZSR}}(\theta_{\text{inc}}) \triangleq \frac{1}{2\pi} \int_0^{2\pi} \frac{G_T(\theta_Z(\theta_{\text{inc}}), \phi)}{G_T(\theta_S(\theta_{\text{inc}}), \phi)} d\phi. \tag{13}$$

In practice, the integral in (13) is performed numerically by averaging over 36 discrete cuts of the patterns in 10° azimuthal increments.

The approximated ZSR is now a function of a single parameter, θ_{inc}, the specular incidence angle. It is evaluated separately for each GPS satellite. The resulting ZSR functions for all GPS satellites are shown in Fig. 4, color coded by block type and antenna design. Commonality in their behavior for a given block type and antenna design can be clearly seen. These ZSR functions were calculated using the prelaunch measured GPS antenna patterns from [51]. For this work, the pattern data were smoothed and interpolated by fitting a power series polynomial to each azimuth cut of the published pattern (36 cuts in total).
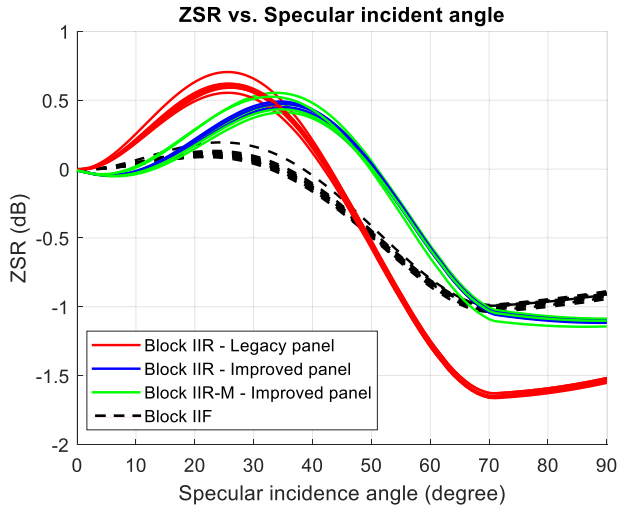
Fig. 4. Calculated ZSR functions for each GPS satellite (grouped based on satellite block type and antenna design).
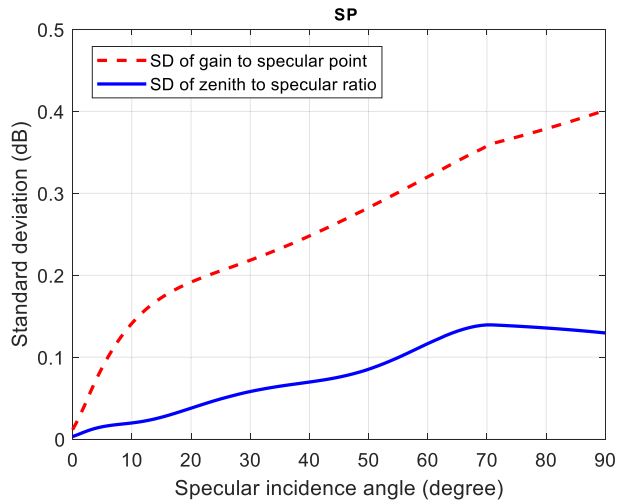

Fig. 5. Standard deviation of the azimuthal variation of the ZSR function (blue) and GPS antenna gain pattern (dashed red) as a function of specular incidence angle.

One key aspect of the ZSR approximation in (13) is that it can be used without knowledge of the GPS satellite yaw state, which is difficult to obtain in practice. The accuracy of the approximation relies on the weak azimuthal dependence of the ZSR function given in (12). To demonstrate the validity of the approximation, Fig. 5 quantifies the azimuthal variation of the ZSR. Although results are only shown for a single GPS satellite, spacecraft vehicle number (SVN) 56, the results for other SVNs are similar. Azimuthal variations in the ZSR (solid blue curve) are characterized by the standard deviation (taken in dB) over all azimuth angles at a particular specular incidence angle. It can be observed that the standard deviation of the error is very small and is ∼0.1 dB or less over most incidence angles. For comparison, Fig. 5 also shows the standard deviation of the GPS antenna gain pattern (dashed red curve), which is mapped to specular incidence angle for comparison with the ZSR function. The standard deviation of the gain pattern can be seen to rise to 0.2 dB at ∼20° incidence and 0.3 dB at ∼55° incidence. If the GPS antenna gain pattern

TABLE II
ERROR ANALYSIS INPUT PARAMETERS

Error Term	1-sigma Error Magnitude
ΔR	10 m
ΔP_z	0.18 dB
ΔG_{LNA}	0.1 dB
ΔG_R	0.2 dB
ΔZSR	0.15 dB

was used directly to estimate EIRP—and if the yaw state of the GPS satellite was not known—these standard deviation values would represent 1-sigma uncertainties in the antenna gain and, ultimately, in the derived science data products. The azimuthal dependence of the ZSR is significantly weaker than that of the antenna gain. For example, at 55° incidence, the standard deviation is ∼0.1 dB, or roughly one-third that of the gain. By using the ZSR function rather than the antenna gain directly, the sensitivity of EIRP estimates to lack of knowledge of the yaw state of a GPS satellite has been reduced by roughly a factor of 3.

F. Estimating GPS EIRP Toward the Specular Point

The estimated GPS satellite EIRP in the specular point direction is calculated as

$$E_S = \frac{E_Z}{\widehat{ZSR}(\theta_{\text{inc}})}. \tag{14}$$

By combining (3), (4), and (14), E_S can be expressed as

$$E_S = \frac{(4\pi R)^2}{\lambda^2} \frac{P_Z}{G_{\text{LNA}}(T_{\text{LNA}})G_R(\theta_R, \phi_R)\widehat{ZSR}(\theta_{\text{inc}})} \tag{15}$$

and is used in the CYGNSS L1b calibration algorithm to estimate NBRCS from the CYGNSS measurements using (1).

IV. ERROR ANALYSIS OF EIRP ESTIMATE

Analysis of the uncertainty associated with estimates of the GPS EIRP is made in two ways, by using a bottom-up decomposition of the estimation algorithm into its component sources of error and by analyzing Monte Carlo trials of the end-to-end computation. In both cases, the individual sources of error are assumed to be independent and uncorrelated. The assumption of independence is likely not strictly valid due, for example, to correlations between some of the errors and variations in the physical temperature of the instrument. Independence is assumed here for simplicity in the initial error analysis, and a more thorough characterization of correlations between the sources of error is left as a topic for future work.

A. Quantifying Error Terms

The terms in (15) which are subject to errors are defined below and their standard deviations are listed in Table II:

1) ΔR : Error in knowledge of the distance between the GPS transmitter and the zenith receiver. This is primarily due to the errors in the accuracy of the positioning.

2) ΔP_z: Error in the converted zenith power at the delay mapping receiver (DMR) input port. This is due to errors in the raw counts C_Z and the second-order polynomial coefficients derived from the EM+GSS calibration experiment.

3) ΔG_{LNA}: Error in the zenith receiver gain. This is due to errors in the measured amplifier temperature and in the prelaunch LUT of gain versus physical temperature.

4) ΔG_R: Error in the zenith antenna gain. This is primarily due to errors in the pattern estimation procedure and in the interpolation process.

5) ΔZSR: Error in the GPS antenna ZSR function. This is due to errors in the gain pattern, the mapping from the GPS off-boresight angles to the specular incidence angle, and the azimuthal variability of ZSR functions. Note that ΔZSR depends on incidence angle and a typical value is selected for the range of incidence angles with the highest density of CYGNSS observables.

B. Root of Sum of Squares (RSS) Error

Using the error analysis approach in [58] and [60], the RSS of the individual error sources can be calculated as

$$\Delta E_S = \left[\sum_{i=1}^{5} [E(q_i)]^2 \right]^{1/2} \quad (16)$$

where q_i is the respective error parameter of the five variables in (15), and the individual error terms can be estimated by taking the partial derivative of the equation, such that each error team can be quantized as

$$E(q_i) = \left| \frac{\partial E_S}{\partial q_i} \right| \Delta q_i \quad (17)$$

where each term can be expressed as

$$E_S(R) = 2R \frac{(4\pi)^2}{\lambda^2} \frac{P_Z}{G_{LNA} G_R} \frac{1}{ZSR} \Delta R \quad (18\text{-a})$$

$$E_S(P_Z) = \frac{(4\pi R)^2}{\lambda^2} \frac{1}{G_{LNA} G_R} \frac{1}{ZSR} \Delta P_Z \quad (18\text{-b})$$

$$E_S(G_{LNA}) = \frac{(4\pi R)^2}{\lambda^2} \frac{P_Z}{G_{LNA}^2 G_R} \frac{1}{ZSR} \Delta G_{LNA} \quad (18\text{-c})$$

$$E_S(G_R) = \frac{(4\pi R)^2}{\lambda^2} \frac{P_Z}{G_{LNA} G_R^2} \frac{1}{ZSR} \Delta G_R \quad (18\text{-d})$$

$$E_S(ZSR) = \frac{(4\pi R)^2}{\lambda^2} \frac{P_Z}{G_{LNA} G_R} \frac{1}{ZSR^2} \Delta ZSR. \quad (18\text{-e})$$

It is noted that the error terms in Table II, except ΔR, are relative errors. Let $\Delta R = \alpha_R R$, $\Delta P_z = \alpha_P P_z$, $\Delta G_{LNA} = \alpha_{GLNA} G_{LNA}$, $\Delta G_R = \alpha_{GR} G_R$, $\Delta ZSR = \alpha_{ZSR} ZSR$, and (18) can be written as

$$E_S(R) = 2\alpha_R E_S \quad (19\text{-a})$$

$$E_S(P_Z) = \alpha_P E_S \quad (19\text{-b})$$

$$E_S(G_{LNA}) = \alpha_{GLNA} E_S \quad (19\text{-c})$$

$$E_S(G_R) = \alpha_{GR} E_S \quad (19\text{-d})$$

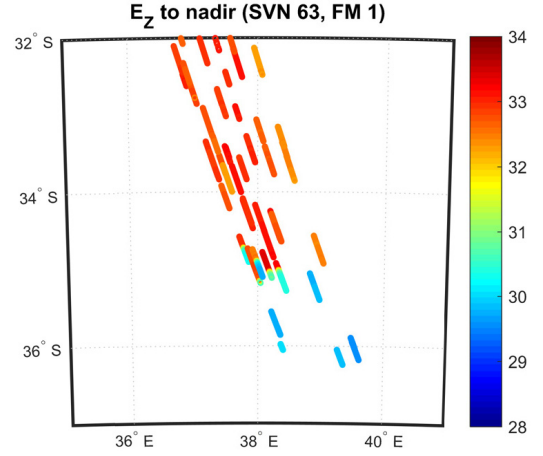$$E_S(ZSR) = \alpha_{ZSR} E_S. \quad (19\text{-e})$$

Fig. 6. EIRP to zenith E_Z estimated using the zenith signal.

Therefore, the relative error of E_S can be calculated as

$$\frac{\Delta E_S}{E_S} = \sqrt{4\alpha_R^2 + \alpha_P^2 + \alpha_{GLNA}^2 + \alpha_{GR}^2 + \alpha_{ZSR}^2}. \quad (20)$$

The error coefficient for the range α_R is calculated using 1 day's data measured by CYGNSS FM 1. Because the range R between GPS and CYGNSS satellites is of the order of 10^7 meter, this error is extremely small. The final RSS error of the EIRP estimate to specular point is 0.3185 dB.

C. Error Estimate Using Monte Carlo Simulation

To independently verify the RSS error approach, a Monte Carlo simulation is also conducted. Error sources are assumed to be independent and uncorrelated. Random noise is generated using a Gaussian distribution with zero-mean and 1-σ uncertainty (error magnitude in Table II). The noise is added to each variable and input to (15) to calculate the model prediction. The population of model outcomes is then analyzed to determine the overall error.

A single estimate of the standard deviation of the specular EIRP, E_S, is derived from 10^6 realizations of (15). This is then repeated 10^4 times and those estimates are averaged together. The final error estimate of E_S using this Monte Carlo approach is 0.3239 dB, which agrees closely with the RSS approach.

D. Error Analysis Discussion

The two approaches to error analysis agree well, with both estimating $\sim$0.32-dB relative error. This reduces the 0.4-dB error term of $E(P_T) + E(G_T)$ in v2.1 Level 1 calibration [58] by about 20%. Besides, the 0.4-dB error does not consider flex power events which can introduce much larger errors, thus the improvement could possibly be larger.

It should be noted that: 1) the error term is dependent on the specular incidence angle because the ZSR function has a dependence on the geometry; 2) there are very small errors caused by the empirical mapping of the two GPS off-boresight angles to the specular incidence angle; and 3) the antenna gain patterns of the CYGNSS zenith antenna and GPS antenna are retrieved using measured direct signal, so there may exist
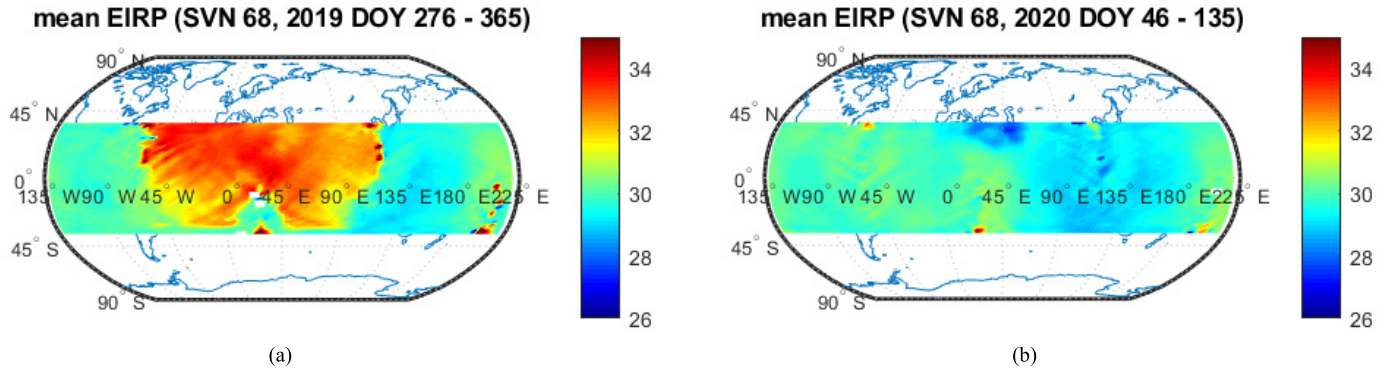
Fig. 7. Average map of estimated EIRP to the specular point of GPS SVN 68. (a) Flex power mode 1, Year 2019 DOY 276–365. (b) Flex power mode 4, Year 2020 DOY 46–135.

interdependent relationships between these variables. These issues will be studied and investigated as future work.

V. CALIBRATION OF GPS EIRP

A. Detection of GPS Flex Power Events

Fig. 6 shows an example of multiple ground tracks of E_Z, the EIRP toward the zenith antenna, for observations by CYGNSS FM 1 of GPS SVN 63 transmissions. The color scale denotes the EIRP in dBW. A flex power change of around 2.5 dB is clearly evident. The repeatability of these flex power events over a long time span demonstrates that it is a geographically driven commanded change, as shown in [54]. This also demonstrates that the CYGNSS zenith signal, as a spaceborne power monitor system, provides a measurement of flex power that is of comparable accuracy to the two ground-based GPS stations.

B. Global Map of GPS EIRP

The geolocation of GPS flex power events can be illustrated by considering the global distribution of EIRP measured by CYGNSS. For Block IIF SVs, there are two flex power modes: mode 1 changes the power of C/A, P(Y), and M codes, while mode 4 changes the P(Y) and M codes but not C/A code [61].

Fig. 7 shows a global map of GPS EIRP to the specular point, E_S, for SVN 68, a Block IIF SV, running in flex power mode 1 (Year 2019, day of year (DOY) 276–365) and 4 (Year 2020, DOY 46-135), respectively. The estimated GPS EIRPs measured by all 8 CYGNSS FMs are binned based on the geolocation of the specular point and averaged in 2° latitude by 4° longitude cells with all specular incidence angles included. In Fig. 7(a), there are distinct levels of EIRP over different regions, which are caused by the flex power mode 1 as described in [61]. This agrees very well with the flex power mode detected by German Aerospace Center (DLR)'s independent measurement in [54]. In Fig. 7(b), when the power of the C/A code does not change with every orbit, the geographical dependence disappears. Note that this EIRP global map is for all specular incidence angles, so it includes the GPS off-boresight angle for the entire range of the Earth service volume (13.8° off-boresight). That causes the variations in the observed EIRP.
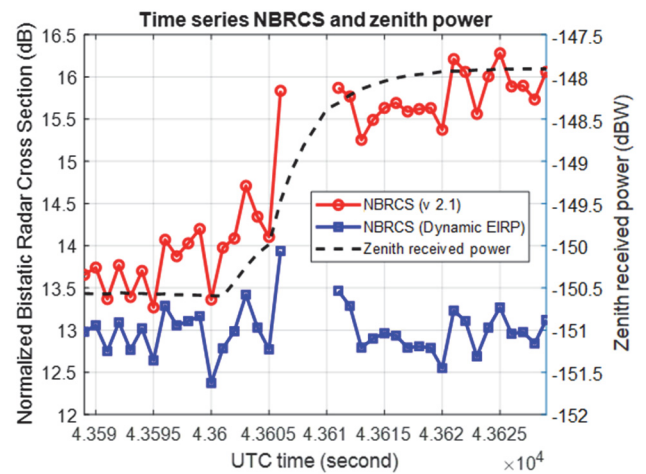

Fig. 8. Case study of the NBRCS calibration during the GPS flex power.

VI. IMPACTS ON CYGNSS LEVEL 1 CALIBRATION

A. Case Study of the GPS Flex Power

An example of the impact of a flex power transition (Year 2018, DOY 213; measured by CYGNSS FM 7) is shown in Fig. 8. The GPS transmit power increases by ∼2.5 dB, as measured by the zenith received power (black dashed line).

In Fig. 8, the nadir science measurements are over open ocean, which has a relatively stable surface wind speed (∼7 m/s). The red line shows the v2.1 calibrated Level 1 NBRCS (using the static LUT for the GPS EIRP estimation) and features an abrupt change as the zenith power changes. The nonphysical behavior of the NRBCS shows that the change in transmit power has not been correctly accounted for. The version 3.0 (v3.0) NBRCS (using the dynamic EIRP calibration) is shown to be insensitive to the change in transmit power. Note that measurements made during a flex power event, when the EIRP is rapidly changing, are flagged and removed by data quality control measures, causing a gap in the NBRCS time series.

B. Time-Series Plot of the Level 1 NBRCS

Fig. 9 presents a time-series daily average of the v3.0 GPS EIRP and NBRCS with signal source of 10 Block IIF SVs operating in the geographically driven flex power mode
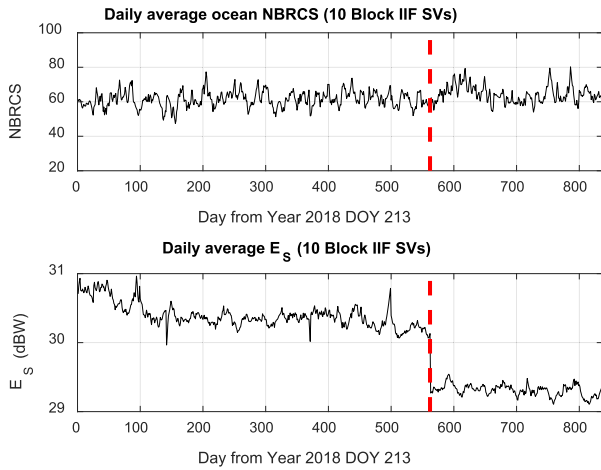
Fig. 9. Time-series daily average of the ocean NBRCS and GPS EIRP measured by CYGNSS using signals transmitted by the 10 Block IIF SVs that were operating in flex power mode during the time period considered.

Fig. 10. Daily coverage of CYGNSS measurements. (a) Without Block IIF data. (b) With Block IIF data.

[54] from Year 2018 DOY 213 to Year 2020 DOY 319. Clearly, when the flex power mode changes from mode 1 to mode 4 on February 14, 2020 (as denoted by the red dashed line), the average GPS EIRP decreases. However, the average NRBCS does not show any significant change. This demonstrated that the Block IIF data are correctly calibrated and can be included in the official Level 1 data products for higher level applications.

C. Improved Daily Coverage With Block IIF Data

Fig. 10 presents a daily coverage map without and with Block IIF data. Clearly, by recovering observations from the GPS Block IIF satellites and including them in the science data products, CYGNSS provides more nearly gap-free measurements for improved science data coverage.

VII. SUMMARY AND FUTURE WORK

A dynamic EIRP calibration approach is proposed to address the calibration issue brought by the flex power mode of the Block IIF and IIR-M satellites. CYGNSS direct signal measurements (originally intended for navigation use only) are calibrated and used to compute GPS transmitter EIRP in the direction of the CYGNSS spacecraft. By applying corrections to the direct signal EIRP, it is possible to estimate the GPS EIRP in the direction of the specular reflection point.

This dynamic EIRP calibration algorithm instantaneously detects and corrects for power fluctuations in all GPS transmitters and significantly reduces errors due to the azimuthal asymmetry of the GPS antenna gain patterns. Error analysis shows that the error in EIRP estimate is about 0.32 dB. The dynamic EIRP calibration successfully detects power fluctuations and corrects them in the calibration of nadir science measurements. This approach allows observations with Block IIF transmitters (approximately 37% of the entire data set) to be included in the standard data products and further improves the calibration quality.

It is useful to analyze the wind speed retrieval errors from measurements taken: 1) in different regions of the zenith antenna p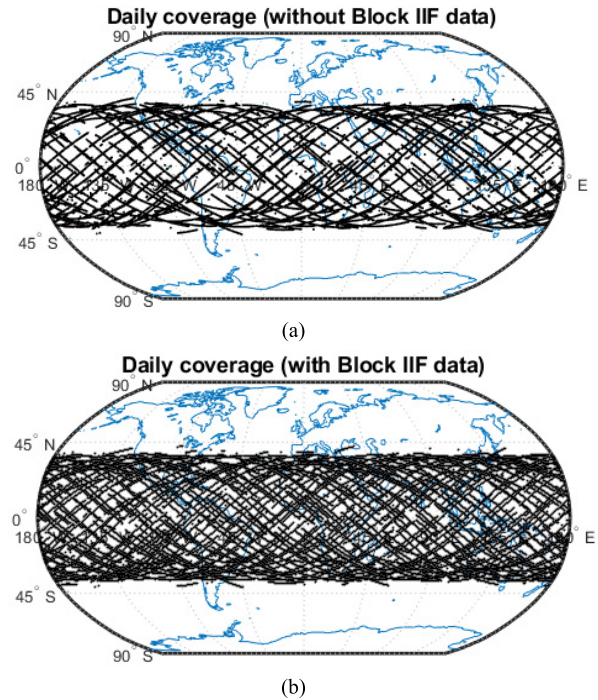attern: higher gain versus lower gain, quadrants, and off-boresight; and 2) in different ranges of the specular incidence angle, which is related to the ZSR function and GPS antenna pattern. Future work includes applying the following improvements: 1) use refined zenith antenna gain pattern and GPS ZSR functions; 2) implement a 2-D ZSR function for EIRP correction, depending on the two off-boresight angles rather than the specular incidence angles (avoiding the empirical mapping); 3) study the long-term variations in the LNA gains and make corresponding corrections; and 4) conduct an error analysis considering the interdependent relationship between the five sources of error.

REFERENCES

[1] B. Hofmann-Wellenhof, H. Lichtenegger, and J. Collins, *Global Positioning System: Theory and Practice*, 5th ed. Vienna, Austria: Springer-Verlag, 2001.

[2] P. Misra and P. Enge, *Global Positioning System: Signals, Measurements, and Performance*, 2nd ed. Lincoln, MA, USA: Ganga-Jamuna Press, 2001.

[3] V. U. Zavorotny, S. Gleason, E. Cardellach, and A. Camps, "Tutorial on remote sensing using GNSS bistatic radar of opportunity," *IEEE Geosci. Remote Sens. Mag.*, vol. 2, no. 4, pp. 8–45, Dec. 2014, doi: 10.1109/MGRS.2014.2374220.

[4] J. L. Garrison, S. J. Katzberg, and M. I. Hill, "Effect of sea roughness on bistatically scattered range coded signals from the global positioning system," *Geophys. Res. Lett.*, vol. 25, no. 13, pp. 2257–2260, Jul. 1998, doi: 10.1029/98GL51615.

[5] B. Lin, S. J. Katzberg, J. L. Garrison, and B. Wielicki, "Relationship between GPS signals reflected from sea surfaces and surface winds: Modeling results and comparisons with aircraft measurements," *J. Geophys. Res.*, vol. 104, no. C9, pp. 20713–20727, Sep. 1999, doi: 10.1029/1999JC900176.

[6] J. L. Garrison, A. Komjathy, V. U. Zavorotny, and S. J. Katzberg, "Wind speed measurement using forward scattered GPS signals," *IEEE Trans. Geosci. Remote Sens.*, vol. 40, no. 1, pp. 50–65, Jan. 2002, doi: 10.1109/36.981349.

[7] A. Komjathy, M. Armatys, D. Masters, P. Axelrad, V. Zavorotny, and S. Katzberg, "Retrieval of ocean surface wind speed and wind direction using reflected GPS signals," *J. Atmos. Ocean. Technol.*, vol. 21, no. 3, pp. 515–526, Mar. 2004, doi: 10.1175/1520-0426(2004)021<0515:ROOSWS>2.0.CO;2.

[8] V. U. Zavorotny and A. G. Voronovich, "Scattering of GPS signals from the ocean with wind remote sensing application," *IEEE Trans. Geosci. Remote Sens.*, vol. 38, no. 2, pp. 951–964, Mar. 2000, doi: 10.1109/36.841977.

[9] S. J. Katzberg, R. A. Walker, J. H. Roles, T. Lynch, and P. G. Black, "First GPS signals reflected from the interior of a tropical storm: Preliminary results from Hurricane Michael," *Geophys. Res. Lett.*, vol. 28, no. 10, pp. 1981–1984, May 2001, doi: 10.1029/2000GL012823.

[10] S. J. Katzberg, O. Torres, and G. Ganoe, "Calibration of reflected GPS for tropical storm wind speed retrievals," *Geophys. Res. Lett.*, vol. 33, no. 18, Sep. 2006, Art. no. L18602, doi: 10.1029/2006GL026825.

[11] S. Gleason *et al.*, "Detection and processing of bistatically reflected GPS signals from low Earth orbit for the purpose of ocean remote sensing," *IEEE Trans. Geosci. Remote Sens.*, vol. 43, no. 6, pp. 1229–1241, Jun. 2005, doi: 10.1109/TGRS.2005.845643.

[12] S. Gleason, "Remote sensing of ocean, ice and land surfaces using bistatically scattered GNSS signals from low earth orbit," Ph.D. dissertation, Dept. Appl. Phys., Univ. Surrey, Guildford, U.K., 2006.

[13] M. Unwin, P. Jales, J. Tye, C. Gommenginger, G. Foti, and J. Rosello, "Spaceborne GNSS-reflectometry on TechDemoSat-1: Early mission operations and exploitation," *IEEE J. Sel. Topics Appl. Earth Observ. Remote Sens.*, vol. 9, no. 10, pp. 4525–4539, Oct. 2016, doi: 10.1109/JSTARS.2016.2603846.

[14] C. Ruf *et al.*, "CYGNSS: Enabling the future of hurricane prediction [remote sensing satellites]," *IEEE Geosci. Remote Sens. Mag.*, vol. 1, no. 2, pp. 52–67, Jun. 2013, doi: 10.1109/MGRS.2013.2260911.

[15] C. S. Ruf *et al.*, "A new paradigm in Earth environmental monitoring with the CYGNSS small satellite constellation," *Sci. Rep.*, vol. 8, no. 1, pp. 1–13, Dec. 2018, doi: 10.1038/s41598-018-27127-4.

[16] H. Carreno-Luengo *et al.*, "3Cat-2—An experimental nanosatellite for GNSS-R Earth observation: Mission concept and analysis," *IEEE J. Sel. Topics Appl. Earth Observ. Remote Sens.*, vol. 9, no. 10, pp. 4540–4551, Oct. 2016, doi: 10.1109/JSTARS.2016.2574717.

[17] C. Jing, X. Niu, C. Duan, F. Lu, G. Di, and X. Yang, "Sea surface wind speed retrieval from the first Chinese GNSS-R mission: Technique and preliminary results," *Remote Sens.*, vol. 11, no. 24, p. 3013, Dec. 2019, doi: 10.3390/rs11243013.

[18] D. Masters *et al.*, "Status and plans for Spire's growing commercial constellation of GNSS science CubeSats," in *Proc. Joint 6th ROM SAF User Workshop 7th IROWG Workshop*, Helsingør, Denmark, Sep. 2019, pp. 19–25.

[19] A. Camps *et al.*, "FSSCat, the 2017 copernicus masters' 'ESA Sentinel small satellite challenge' Winner: A federated polar and soil moisture tandem mission based on 6U cubesats," in *Proc. IEEE Int. Geosci. Remote Sens. (IGARSS)*, Valencia, Spain, Jul. 2018, pp. 8285–8287, doi: 10.1109/IGARSS.2018.8518405.

[20] M. P. Clarizia, C. Ruf, P. Cipollini, and C. Zuffada, "First spaceborne observation of sea surface height using GPS-reflectometry," *Geophys. Res. Lett.*, vol. 43, no. 2, pp. 767–774, Jan. 2016, doi: 10.1002/2015GL066624.

[21] E. Cardellach *et al.*, "First precise spaceborne sea surface altimetry with GNSS reflected signals," *IEEE J. Sel. Topics Appl. Earth Observ. Remote Sens.*, vol. 13, pp. 102–112, 2020. [Online]. Available: https://ieeexplore.ieee.org/document/8945180, doi: 10.1109/JSTARS.2019.2952694.

[22] B. Annane, B. McNoldy, S. M. Leidner, R. Hoffman, R. Atlas, and S. J. Majumdar, "A study of the HWRF analysis and forecast impact of realistically simulated CYGNSS observations assimilated as scalar wind speeds and as VAM wind vectors," *Monthly Weather Rev.*, vol. 146, no. 7, pp. 2221–2236, Jul. 2018, doi: 10.1175/MWR-D-17-0240.1.

[23] S. M. Leidner, B. Annane, B. McNoldy, R. Hoffman, and R. Atlas, "Variational analysis of simulated ocean surface winds from the Cyclone Global Navigation Satellite System (CYGNSS) and evaluation using a regional OSSE," *J. Atmos. Ocean. Technol.*, vol. 35, no. 8, pp. 1571–1584, Aug. 2018, doi: 10.1175/JTECH-D-17-0136.1.

[24] D. Mayers and C. Ruf, "Tropical cyclone center fix using CYGNSS winds," *J. Appl. Meteorol. Climatol.*, vol. 58, no. 9, pp. 1993–2003, Sep. 2019, doi: 10.1175/JAMC-D-19-0054.1.

[25] G. Foti *et al.*, "Spaceborne GNSS reflectometry for ocean winds: First results from the UK TechDemoSat-1 mission," *Geophys. Res. Lett.*, vol. 42, no. 13, pp. 5435–5441, Jul. 2015, doi: 10.1002/2015GL064204.

[26] M. P. Clarizia and C. S. Ruf, "Wind speed retrieval algorithm for the Cyclone Global Navigation Satellite System (CYGNSS) mission," *IEEE Trans. Geosci. Remote Sens.*, vol. 54, no. 8, pp. 4419–4432, Aug. 2016, doi: 10.1109/TGRS.2016.2541343.

[27] A. Ghavidel and A. Camps, "Impact of rain, swell, and surface currents on the electromagnetic bias in GNSS-reflectometry," *IEEE J. Sel. Topics Appl. Earth Observ. Remote Sens.*, vol. 9, no. 10, pp. 4643–4649, Oct. 2016, doi: 10.1109/JSTARS.2016.2538181.

[28] S. Soisuvarn, Z. Jelenak, F. Said, P. S. Chang, and A. Egido, "The GNSS reflectometry response to the ocean surface winds and waves," *IEEE J. Sel. Topics Appl. Earth Observ. Remote Sens.*, vol. 9, no. 10, pp. 4678–4699, Oct. 2016, doi: 10.1109/JSTARS.2016.2602703.

[29] B. Li, L. Yang, B. Zhang, D. Yang, and D. Wu, "Modeling and simulation of GNSS-R observables with effects of swell," *IEEE J. Sel. Topics Appl. Earth Observ. Remote Sens.*, vol. 13, pp. 1833–1841, 2020. [Online]. Available: https://ieeexplore.ieee.org/document/9086069, doi: 10.1109/JSTARS.2020.2992037.

[30] A. Camps *et al.*, "Sensitivity of GNSS-R spaceborne observations to soil moisture and vegetation," *IEEE J. Sel. Topics Appl. Earth Observ. Remote Sens.*, vol. 9, no. 10, pp. 4730–4742, Oct. 2016, doi: 10.1109/JSTARS.2016.2588467.

[31] C. C. Chew and E. E. Small, "Soil moisture sensing using spaceborne GNSS reflections: Comparison of CYGNSS reflectivity to SMAP soil moisture," *Geophys. Res. Lett.*, vol. 45, no. 9, pp. 4049–4057, May 2018, doi: 10.1029/2018GL077905.

[32] M. M. Al-Khaldi, J. T. Johnson, A. J. O'Brien, A. Balenzano, and F. Mattia, "Time-series retrieval of soil moisture using CYGNSS," *IEEE Trans. Geosci. Remote Sens.*, vol. 57, no. 7, pp. 4322–4331, Jul. 2019, doi: 10.1109/TGRS.2018.2890646.

[33] M. P. Clarizia, N. Pierdicca, F. Costantini, and N. Floury, "Analysis of CYGNSS data for soil moisture retrieval," *IEEE J. Sel. Topics Appl. Earth Observ. Remote Sens.*, vol. 12, no. 7, pp. 2227–2235, Jul. 2019, doi: 10.1109/JSTARS.2019.2895510.

[34] H. Carreno-Luengo, G. Luzi, and M. Crosetto, "Above-ground biomass retrieval over tropical forests: A novel GNSS-R approach with CyGNSS," *Remote Sens.*, vol. 12, no. 9, p. 1368, Apr. 2020, doi: 10.3390/RS12091368.

[35] A. Camps, A. Alonso-Arroyo, H. Park, R. Onrubia, D. Pascual, and J. Querol, "L-band vegetation optical depth estimation using transmitted GNSS signals: Application to GNSS-reflectometry and positioning," *Remote Sens.*, vol. 12, no. 15, p. 2352, Jul. 2020, doi: 10.3390/RS12152352.

[36] K. Jensen, K. McDonald, E. Podest, N. Rodriguez-Alvarez, V. Horna, and N. Steiner, "Assessing L-band GNSS-reflectometry and imaging radar for detecting sub-canopy inundation dynamics in a tropical wetlands complex," *Remote Sens.*, vol. 10, no. 9, p. 1431, Sep. 2018, doi: 10.3390/rs10091431.

[37] C. Chew and E. Small, "Estimating inundation extent using CYGNSS data: A conceptual modeling study," *Remote Sens. Environ.*, vol. 246, Sep. 2020, Art. no. 111869, doi: 10.1016/j.rse.2020.111869.

[38] S. V. Nghiem *et al.*, "Wetland monitoring with global navigation satellite system reflectometry," *Earth Space Sci.*, vol. 4, no. 1, pp. 16–39, Jan. 2017, doi: 10.1002/2016EA000194.

[39] M. Morris, C. Chew, J. T. Reager, R. Shah, and C. Zuffada, "A novel approach to monitoring wetland dynamics using CYGNSS: Everglades case study," *Remote Sens. Environ.*, vol. 233, Nov. 2019, Art. no. 111417, doi: 10.1016/j.rse.2019.111417.

[40] A. Alonso-Arroyo, V. U. Zavorotny, and A. Camps, "Sea ice detection using U.K. TDS-1 GNSS-R data," *IEEE Trans. Geosci. Remote Sens.*, vol. 55, no. 9, pp. 4989–5001, Sep. 2017, doi: 10.1109/TGRS.2017.2699122.

[41] Q. Yan and W. Huang, "Sea ice thickness measurement using spaceborne GNSS-R: First results with TechDemoSat-1 data," *IEEE J. Sel. Topics Appl. Earth Observ. Remote Sens.*, vol. 13, pp. 577–587, 2020. [Online]. Available: https://ieeexplore.ieee.org/document/8966611, doi: 10.1109/JSTARS.2020.2966880.

[42] A. Rius, E. Cardellach, F. Fabra, W. Li, S. Ribó, and M. Hernández-Pajares, "Feasibility of GNSS-R ice sheet altimetry in Greenland using TDS-1," *Remote Sens.*, vol. 9, no. 7, p. 742, Jul. 2017, doi: 10.3390/rs9070742.

[43] W. Li, E. Cardellach, F. Fabra, S. Ribó, and A. Rius, "Measuring Greenland ice sheet melt using spaceborne GNSS reflectometry from TechDemoSat-1," *Geophys. Res. Lett.*, vol. 47, no. 2, Jan. 2020, Art. no. e2019GL086477, doi: 10.1029/2019GL086477.

[44] S. Gleason, "Space-based GNSS scatterometry: Ocean wind sensing using an empirically calibrated model," *IEEE Trans. Geosci. Remote Sens.*, vol. 51, no. 9, pp. 4853–4863, Sep. 2013, doi: 10.1109/TGRS.2012.2230401.

[45] M. Asgarimehr, J. Wickert, and S. Reich, "TDS-1 GNSS reflectometry: Development and validation of forward scattering winds," *IEEE J. Sel. Topics Appl. Earth Observ. Remote Sens.*, vol. 11, no. 11, pp. 4534–4541, Nov. 2018, doi: 10.1109/JSTARS.2018.2873241.

[46] C. S. Ruf and R. Balasubramaniam, "Development of the CYGNSS geophysical model function for wind speed," *IEEE J. Sel. Topics Appl. Earth Observ. Remote Sens.*, vol. 12, no. 1, pp. 66–77, Jan. 2019, doi: 10.1109/JSTARS.2018.2833075.

[47] C. S. Ruf, S. Gleason, and D. S. McKague, "Assessment of CYGNSS wind speed retrieval uncertainty," *IEEE J. Sel. Topics Appl. Earth Observ. Remote Sens.*, vol. 12, no. 1, pp. 87–97, Jan. 2019, doi: 10.1109/JSTARS.2018.2825948.

[48] S. Gleason, C. S. Ruf, A. J. O'Brien, and D. S. McKague, "The CYGNSS level 1 calibration algorithm and error analysis based on on-orbit measurements," *IEEE J. Sel. Topics Appl. Earth Observ. Remote Sens.*, vol. 12, no. 1, pp. 37–49, Jan. 2019, doi: 10.1109/JSTARS.2018.2832981.

[49] T. Wang, C. Ruf, B. Block, D. McKague, and S. Gleason, "Characterization of GPS L1 EIRP: Transmit power and antenna gain pattern," in *Proc. 31st Int. Tech. Meeting Satell. Division Inst. Navigat. (ION GNSS+)*, Miami, FL, USA, 2018, pp. 2879–2890, doi: 10.33012/2018.16101.

[50] T. Wang, C. S. Ruf, B. Block, D. S. McKague, and S. Gleason, "Design and performance of a GPS constellation power monitor system for improved CYGNSS L1B calibration," *IEEE J. Sel. Topics Appl. Earth Observ. Remote Sens.*, vol. 12, no. 1, pp. 26–36, Jan. 2019, doi: 10.1109/JSTARS.2018.2867773.

[51] W. A. Marquis and D. L. Reigh, "The GPS block IIR and IIR-M broadcast L-band antenna panel: Its pattern and performance," *Navigat., J. Inst. Navigat.*, vol. 62, no. 4, pp. 329–347, Winter 2015, doi: 10.1002/navi.123.

[52] F. Said, Z. Jelenak, P. S. Chang, and S. Soisuvarn, "An assessment of CYGNSS normalized bistatic radar cross section calibration," *IEEE J. Sel. Topics Appl. Earth Observ. Remote Sens.*, vol. 12, no. 1, pp. 50–65, Jan. 2019, doi: 10.1109/JSTARS.2018.2849323.

[53] P. Steigenberger, A. Hauschild, S. Thoelert, and R. B. Langley, "US air force puts more power into GPS block IIR-M C/A-code," *GPS World*, vol. 28, no. 4, pp. 8–9, Apr. 2017.

[54] P. Steigenberger, S. Thölert, and O. Montenbruck, "Flex power on GPS block IIR-M and IIF," *GPS Solutions*, vol. 23, no. 1, pp. 1–12, Jan. 2019, doi: 10.1007/s10291-018-0797-8.

[55] T. Wang, C. Ruf, S. Gleason, B. Block, D. McKague, and A. O'Brien, "A real-time EIRP level 1 calibration algorithm for the CYGNSS mission using the zenith measurements," in *Proc. IEEE Int. Geosci. Remote Sens. Symp. (IGARSS)*, Yokohama, Jpn., Jul./Aug. 2019, pp. 8725–8728, doi: 10.1109/IGARSS.2019.8900456.

[56] Y. E. Bar-Sever, "A new model for GPS yaw attitude," *J. Geodesy*, vol. 70, pp. 714–723, Nov. 1996, doi: 10.1007/BF00867149.

[57] S. Desai *et al. GNSS-Inferred Positioning System and Orbit Analysis Simulation Software (GYPSY-OASIS)*. Internet. Accessed: Jan. 2018. [Online]. Available: https:// gipsy-oasis.jpl.nasa.gov/

[58] S. Gleason, C. S. Ruf, M. P. Clarizia, and A. J. O'Brien, "Calibration and unwrapping of the normalized scattering cross section for the cyclone global navigation satellite system," *IEEE Trans. Geosci. Remote Sens.*, vol. 54, no. 5, pp. 2495–2509, May 2016, doi: 10.1109/TGRS.2015.2502245.

[59] T. Wang *et al.*, "Measurement of GPS and CYGNSS antenna gain patterns with a spaceborne antenna range," *IEEE Trans. Antennas Propag.*, to be published.

[60] S. J. Keihm, "TOPEX/poseidon microwave radiometer (TMR). II. Antenna pattern correction and brightness temperature algorithm," *IEEE Trans. Geosci. Remote Sens.*, vol. 33, no. 1, pp. 138–146, Jan. 1995, doi: 10.1109/36.368214.

[61] P. Steigenberger, S. Thoelert, O. Esenbuga, A. Hauschild, and O. Montenbruck, "The new flex power mode: From GPS IIR-M and IIF satellites with extended coverage area," *Inside GNSS*, vol. 15, no. 3, pp. 52–56, 2020.

Tianlin Wang (Member, IEEE) received the B.E. degree in electrical engineering from the East China University of Science and Technology, Shanghai, China, in 2009, the M.S. degree in radio physics from Fudan University, Shanghai, China, in 2012, and the M.S. and Ph.D. degrees in electrical engineering from the University of Michigan, Ann Arbor, MI, USA, in 2019 and 2021, respectively.

His research work contributed to engineering calibration and geophysical retrieval for the Cyclone Global Navigation Satellite System NASA Earth Venture Mission. His research interests include microwave remote sensing, microwave measurements, and radio frequency (RF) circuits.

Dr. Wang is a member of Tau Beta Pi, Eta Kappa Nu, American Geophysical Union (AGU), and Institute of Navigation (ION) and an Early Career Member of Commission F of the U.S. National Committee (USNC) for the Union Radio Scientifique Internationale (URSI). He was a recipient of the 2018 IEEE Mikio Takagi Student Prize, the Outstanding Student Presentation Award at 2018 AGU Fall Meeting, the 2020 Richard F. and Eleanor A. Towner Prize for Distinguished Academic Achievement and Distinguished Leadership Award from the University of Michigan, and the 2021 Ernest K. Smith USNC-URSI Student Prize (Second Place).

Christopher S. Ruf (Fellow, IEEE) received the B.A. degree in physics from Reed College, Portland, OR, USA, in 1982, and the Ph.D. degree in electrical and computer engineering from the University of Massachusetts at Amherst, Amherst, MA, USA, in 1987.

He is the Frederick Bartman Collegiate Professor of climate and space science with the University of Michigan and Principal Investigator of the NASA Cyclone Global Navigation Satellite System Mission. He has worked previously at Intel Corporation, Hughes Space and Communication, the NASA Jet Propulsion Laboratory, Pasadena, CA, USA, and Penn State University, State College, PA, USA. His research interests include GNSS-R remote sensing, microwave radiometry, atmosphere and ocean geophysical retrieval algorithm development, and sensor technology development.

Dr. Ruf is a member of the American Geophysical Union, the American Meteorological Society, and Commission F of the Union Radio Scientifique Internationale. He was a recipient of the 1997 IEEE TGRS Best Paper Award, the 1999 IEEE Resnik Technical Field Award, the 2006 IGARSS Best Paper Award, the 2014 IEEE GRSS Outstanding Service Award, the 2017 AIAA SmallSat Mission of the Year Award, and the 2020 University of Michigan Distinguished Faculty Achievement Award. He is a former Editor-in-Chief of the IEEE TRANSACTIONS ON GEOSCIENCE AND REMOTE SENSING and has served on the editorial boards of *Radio Science*, the *Journal of Atmospheric and Oceanic Technology*, and *Nature Scientific Reports*.

Scott Gleason (Senior Member, IEEE) received the B.S. degree in electrical and computer engineering from the State University of New York at Buffalo, Buffalo, NY, USA, in 1991, the M.S. degree in engineering from Stanford University, Stanford, CA, USA, in 1999, and the Ph.D. degree in applied physics from the University of Surrey, Surrey, U.K., in 2007.

He is a Project Scientist III with the University Corporation for Atmospheric Research, Boulder, CO, USA. He is a Co-Investigator on the science team and Instrument Scientist for the NASA CYGNSS Mission. He has worked in the areas of astronautics, remote sensing, and global navigation satellite systems for more than 20 years, including at NASA's Goddard Space Flight Center, Greenbelt, MD, USA, Stanford's GPS Laboratory, Stanford, Surrey Satellite Technology Ltd, Guildford, U.K., Concordia University, Montréal, QC, USA, and the National Oceanography Centre, Southampton, U.K.

Andrew J. O'Brien (Member, IEEE) has worked in the area of adaptive GNSS antenna arrays and precision GNSS receiver algorithms for over a decade. He is a Research Scientist with the ElectroScience Laboratory, Department of Electrical and Computer Engineering, The Ohio State University, Columbus, OH, USA. His primary research focus is spaceborne GNSS remote sensing using CYGNSS, TDS-1, and soil moisture active passive (SMAP). His other research activities include GNSS antenna arrays, antenna electronics, electromagnetic simulation, and radar systems.

Dr. O'Brien is a member of the CYGNSS Science Team and supported the development of CYGNSS end-to-end simulator and CYGNSS engineering activities.

Bruce P. Block received the B.S. degree in electrical engineering from the University of Michigan, Ann Arbor, MI, USA, in 1975.

He is a former Lead Engineer in research with the Space Physics Research Laboratory, College of Engineering, University of Michigan, where he developed hardware and software for ground testing of the CYGNSS Delay Doppler Mapping Instrument. In addition to his interests in Global Navigation Satellite System technology for geodesy and remote sensing, he has, over the course of 40 years, developed numerous electro-mechanical designs for spaceborne mass spectrometry, Langmuir probe, and gas chromatography instruments in collaboration with NASA's Goddard Space Flight Center, Jet Propulsion Laboratory, and Marshall Space Flight Center; JHU Applied Physics Laboratory; and the European Space Agency.

Darren S. McKague (Member, IEEE) received the Ph.D. degree in astrophysical, planetary, and atmospheric sciences from the University of Colorado, Boulder, CO, USA, in 2001.

He worked as a Systems Engineer for Ball Aerospace and for Raytheon and as a Research Scientist with Colorado State University, Fort Collins, CO, USA. He is an Associate Research Scientist with the Department of Climate and Space Sciences and Engineering, University of Michigan, Ann Arbor, MI, USA. His work has focused on remote sensing with emphases on the development of space-borne microwave remote sensing hardware, microwave remote sensor calibration techniques, and mathematical inversion techniques for geophysical retrievals. He is part of the CYGNSS science team, working on calibration/validation of the CYGNSS Level 1 and 2 products, as well as part of the CYGNSS Project Management Team.

Anthony Russel received the B.S. degree in computer science engineering from Michigan State University, East Lansing, MI, USA, in 2014.

He is a member of the engineering staff with the Space Physics Research Laboratory, College of Engineering, University of Michigan, Ann Arbor, MI, USA. His primary engineering activities involve algorithm development and large-scale data processing as a member of the Science Operations Center for the CYGNSS mission.